A Modeling Approach to Account for Unstable Stratification, Flow Acceleration, and Variable Thermophysical Properties for Supercritical Carbon Dioxide

Saad A. Jajja[a], Lindsey V. Randle[a], Brian M. Fronk[a,*]

[a]*School of Mechanical, Industrial and Manufacturing Engineering*
Oregon State University
Corvallis, OR 97331 USA

Abstract

A first of its kind reduced-order predictive heat transfer model is developed to account for the effects of unstable stratification, flow acceleration, and variable thermophysical properties for supercritical carbon dioxide. These phenomena govern thermal transport in the proximity of the pseudo-critical point when the applied heating is limited to the bottom wall of the flow channel. The reduced order model assumes two-dimensional thermal transport and involves the iterative solution of the turbulent Prandtl number. The predictions of this model were compared against experimental data. Out of a total of 16 test data sets, each comprising over 200 individual data points, the model was able to predict 14 data sets with a mean average percent error ($MAPE$) of less than 20%. Additionally, a heat transfer design correlation is proposed which can predict the experimental data with a $MAPE$ of less than

*Corresponding author
Email address: brian.fronk@oregonstate.edu (Brian M. Fronk)

Preprint submitted to International Journal of Heat and Mass Transfer *June 1, 2022*

22%. The modeling approaches outlined in this work provide an alternative to using CFD to model coupled and counteracting phenomena that governs thermal transport for supercritical fluids in asymmetrically bottom heated ducts.
Keywords: Supercritical, Carbon Dioxide, Heat Transfer, Single Wall Heating, Turbulent Flow, Microchannel, Reduced Order Model

---

1. Introduction and Prior Work

Over the past decades, several heat transfer models have been proposed to predict thermal transport in the proximity of the pseudo-critical point for supercritical fluids [1, 2, 3]. These models were primarily developed to predict heat transfer of supercritical fluids in vertically oriented, macroscale, and uniformly heated geometries—representative of the operating conditions experienced in the nuclear power generation industry [4, 5]. Fluid could either be flowing against or along the direction of the gravity vector. Several authors reported sharp peaks in the wall temperature for supercritical fluid flows in an upward direction, whereas such peaks were absent for fluid flowing in a downward direction. A summary of these results can be found in [1].

The proposed models in [1, 2, 3] attributed these observations to the influence of transverse and axial density gradients in altering the shear stress distribution in the flow field. This change in stress distribution was then related to the heat transfer via the Reynolds analogy. Additionally, these models also account for the variation in the thermophysical properties across the boundary layer by using various property ratio terms, e.g. $\left(\frac{\mu_{bulk}}{\mu_{wall}}\right)^x$. While these models have been successful in predicting heat transfer for uniformly heated vertical geometries, it is unclear if these models apply to applications where the applied heating is non-uniform and non-circular microchannel based geometries are used. These applications can include microchannel based heat exchangers in solar thermal applications [6, 7], thermal management of high heat fluxes [8, 9] or in cooling of gas turbine blades.

In our recent work [10], we designed and fabricated a test section in which the flow channels were subjected to extreme asymmetry in applied heating. Figure 1 shows the schematic of the test section, with dimensions shown in Table 1. Inconel 718 formed the bottom wall of the flow channels while the remainder of the flow channel walls were of a thermally and electrically insulating material, Torlon. The heat flux boundary was applied by Joule heating the Inconel-718 and the resulting surface temperatures were measured using an infrared camera.

Table 1: Dimensions of the microchannel test section from [10]

Nomenclature	Description	Numerical value
Th_{BW}	Thickness of the Inconel sheet	254 μm
L_{ch}	Length of the flow channel	50 mm
H_{ch}	Height of the flow channel	600 μm
W_{ch}	Width of the flow channel	2 mm
N_{ch}	Number of flow channels	3
Th_{SW}	Thickness of the channel side wall	1.5 mm
Th_{OE}	Thickness of the outer edge	1.5 mm
$L_{Inconel}$	Total length of the Inconel sheet	64 mm
$W_{Inconel}$	Total width of the Inconel sheet	13 mm

Using this setup, experiments were conducted for a range of inlet mass flux ($430 \leq G \leq 800$ kg m^{-2} s^{-1}), applied heat flux ($5.7 \leq q'' \leq 14.12$ W cm^{-2}), inlet temperature ($31 \leq T_{in} \leq 32.9$ °C) and at a reduced pressure of 1.04. We found that the existing heat transfer models did not predict our experimental data well (Average $MAPE > 100\%$). For these conditions, unstable stratification, flow acceleration, and variable thermophysical properties governed thermal transport. Two factors can be used to explain the inability of existing design correlations to predict the heat transfer for single wall heating boundary conditions.

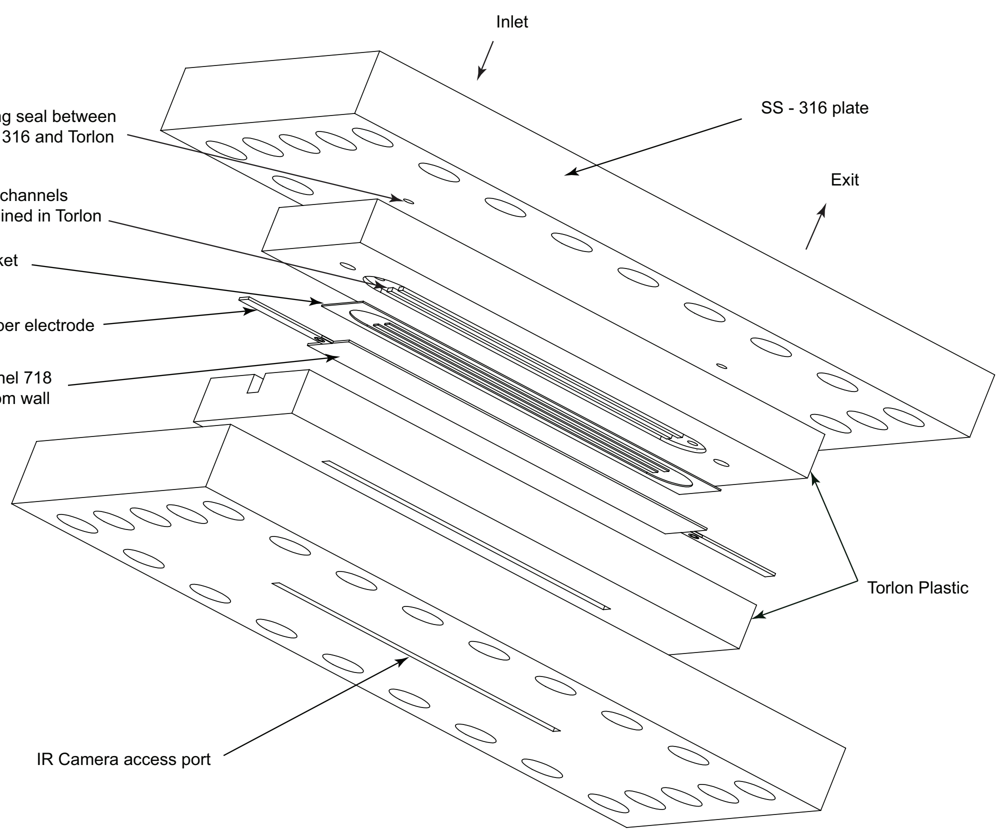

Figure 1: Exploded view of the test section showing sub-components [10].

Existing models, developed for uniformly heated ducts, account for unstable and stable stratification existing simultaneously in the flow channels. This is not the case when the applied heat flux is limited to a single wall of the flow channel. Additionally, regardless of the presence of buoyancy or flow acceleration effects, asymmetric heating can also compromise the predictive capability of existing models developed for uniform heating. Heat transfer coefficients associated with a fluid in a channel with a single wall heated can be lower than the case where all walls are uniformly heated. This has been reported for sub-critical single-phase turbulent fluid flows [11].

With no existing models for asymmetric heating in horizontal operating conditions, thermal engineers must rely on computational fluid dynamics (CFD) simulations to help with sizing the heat exchangers. These simulations can be computationally expensive, and more importantly, the results of such simulations have not been validated against local experimental heat transfer data. Recently, Nabil and Rattner [9] used CFD to predict heat transfer for supercritical fluids in asymmetrically heated ducts. Due to the lack of availability of local heat transfer data, they instead used average experimental data from our previous study [12] for validation purposes. It is not clear if these models can accurately predict local heat transfer. Accurate prediction of local heat transfer is crucial to avoid local hot-spots formation which can be detrimental for device performance, such as in electronics cooling applications.

To address these shortcomings, this study (1) provides empirical evidence of buoyancy effects in non-uniformly heated microchannels, which established the need to model unstable stratification effects in bottom heated microchannels, (2) introduces a reduced order modeling framework that can predict the local heat transfer of sCO_2 in the proximity of the pseudo-critical point when the applied heating is limited to the bottom wall of the flow channel, and (3) presents an easy to implement design correlation that can be used to size microchannel devices using sCO_2.. The model and design correlation are validated using the bottom heated experimental data obtained from the test section developed in our previous work [10]. The tabulated data used for comparison are publicly available in compiled form in [13].

The model and correlation developed in this study are for single-wall, bottom heating configuration. This is an extreme case for asymmetric heating and their predictions will provide a conservative estimate for varying degree of asymmetry in applied heating.

2. Evidence for Presence of Buoyancy Effects in Microchannels

In our earlier work [10], transition criteria suggested that buoyancy effects were expected to be important for certain conditions in horizontal microchannels, but empirical evidence for the presence of stratification was not presented. Since the modeling methodology presented in the later sections will account for these effects, using the same test section, we conducted additional experiments to obtain this empirical evidence. The details of these experiments can be found in Randle and Fronk [14], however a brief summary is provided here.

In these experiments, the test section was operated in a top heated configuration and a bottom heated configuration for the same nominal inlet and heat flux boundary conditions. The resulting surface temperatures of the channel wall were measured and the local heat transfer coefficients were calculated. These results are shown in Figure 2. In this comparison, the increase in the heat transfer coefficients in the final 10 mm length of the channel was ignored. This is because the more effective cooling in the exit header region influences the surface temperature in the final portion of the flow channel. Details of the channel design, validation of the experimental approach, and detailed uncertainty analysis are reported in [10].

Generally, the local heat transfer coefficients for the top heated configuration are lower compared to the bottom heated configuration. In the majority of the developed length segment ($\geq$ 19 mm), this deviation is not within experimental uncertainty. On average, the heat transfer coefficients for the top heated configuration are 16% and 13.9% lower than the bottom heated configuration for an applied heat flux of 7.2 W cm^{-2} and 11.1 W cm^{-2}, respectively. This difference in the heat transfer coefficients for these two operating orientations confirms the presence of stratification and therefore its effects should be accounted for in a mechanistic heat transfer model.

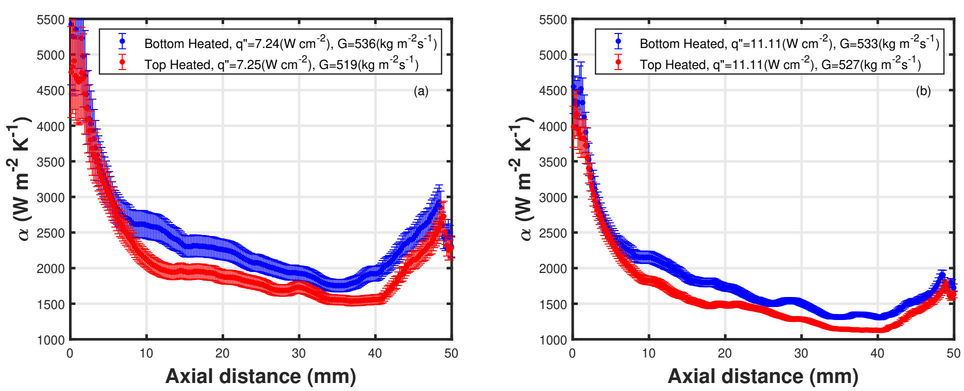

Figure 2: Comparison of local heat transfer coefficients for two different test section orientations. (a) Nominal Mass flux is 520 kg m^{-2} s^{-1} and nominal heat flux is 7.2 W cm^{-2}. (b) Nominal Mass flux is 520 kg m^{-2} s^{-1} and nominal heat flux is 11.1 W cm^{-2}.

3. Modeling Methodology

The flow channel geometry with heating limited to a single wall is modeled as flow between two parallel plates. This assumes that the thermal transport in the channel is a two-dimensional phenomena. Figure 3 shows the modeling domain.

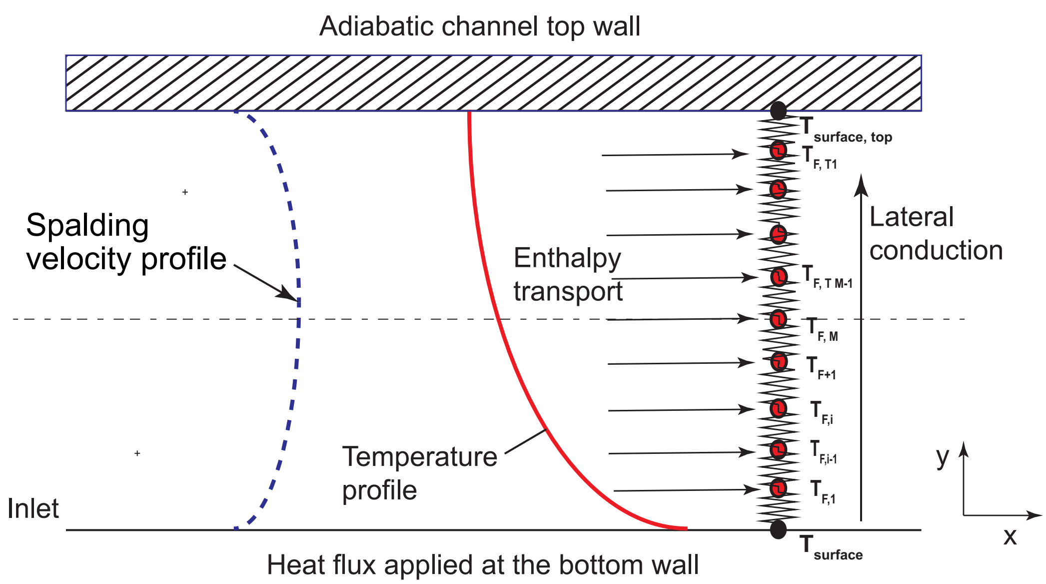

Figure 3: Schematic of the modeled channel flow geometry. This analysis assumes two-dimensional heat transfer between parallel plates.

For this domain, the energy equation for the boundary layer can be greatly simplified by ignoring the effects of axial conduction in the fluid stream and viscous dissipation. Additionally, by assuming steady and fully developed flow conditions, the resulting equation is represented by Eq. (1) — a balance between the enthalpy carried by the fluid stream and the lateral conduction into the fluid stream. Here, the effective conductivity (k_{eff}) is accounting for both molecular and turbulent transport mechanisms, as shown in Eq. (2).

$$\rho c u \frac{\delta T}{\delta x} = k_{eff} \frac{\delta^2 T}{\delta y^2} \tag{1}$$

$$k_{eff} = k_{mol} + \frac{\nu \rho c}{Pr_{turb}} \left(\frac{\sigma_m}{\nu} \right) \tag{2}$$

The influence of bulk flow acceleration on turbulent thermal conductivity can be accounted for by using the Van-Driest expression for eddy diffusivity, shown in Eq. (3). In this expression for eddy diffusivity, A^+ is the effective viscous sub-layer thickness and is expressed by Eq. (5), and adapted from [15]. The effects of the axial pressure gradient on the viscous sub-layer thickness are accounted for by P^+, which is negative for favorable pressure gradients.

$$\frac{\sigma_m}{\nu} = \left[\kappa y^+ \left(1 - e^{-\frac{y^+}{A^+}} \right) \right]^2 \left| \frac{du^+}{dy^+} \right| \tag{3}$$

$$\frac{du^+}{dy^+} = \frac{1}{1 + \frac{\sigma_m}{\nu}} \tag{4}$$

$$A^+ = \frac{25.0}{7.1 \left[4.25(p^+) \right] + 1} \tag{5}$$

$$p^+ = \frac{\mu_{wall} \frac{dP}{dx}}{\rho^{\frac{1}{2}} \tau_s^{\frac{3}{2}}} \tag{6}$$

Unstable stratification in the channel will tend to enhance the eddy diffusivity of heat compared to that of momentum [16]. This enhancement can be accounted for by using the appropriate value of the turbulent Prandtl number, defined in Eq. (7). The methodology to calculate the turbulent Prandtl number is presented in Section 3.2

$$Pr_{turb} = \frac{\frac{\sigma_m}{\nu}}{\frac{\sigma_H}{\nu}} \tag{7}$$

Numerical solution of the simplified energy equation requires two boundary conditions across the y-coordinate (channel height) and an initial condition in the x-coordinate. The boundary condition at the channel bottom wall is that of the uniform heat flux, while an adiabatic boundary condition is assumed at the channel top wall. The inlet bulk fluid temperature is used as an initial condition in the x-coordinate. With the two-dimensional fluid temperature and the channel bottom wall temperature known, the local heat transfer coefficient and Nusselt number can be evaluated. The fluid domain can be discretized by using a resistance network based approach as shown in Figure 3.

To model the enthalpy transport through these fluid nodes, the velocity distribution in the channel needs to be defined. In this model, it is assumed that buoyancy and flow acceleration are not affecting the velocity profile, which is consistent with the assumption of hydrodynamically fully developed flow conditions. The limitation of this assumption is discussed in Section 4.1. To obtain the velocity distribution across the flow channel, the turbulent velocity profile proposed by Spalding [17] was used. This expression, shown in Eq. (8), represents the non-dimensional velocity distribution from the wall to the center of the flow channel. By assuming a symmetric velocity profile, the same distribution can be assumed to exist in the upper half of the flow channel.

$$y^+ = u^+ + 0.11408\left[e^{(\kappa u^+)} - 1 - \kappa u^+ - \frac{(\kappa u^+)^2}{2} - \frac{(\kappa u^+)^3}{6} - \frac{(\kappa u^+)^4}{24}\right] \quad (8)$$

Using this non-dimensional velocity profile, dimensional velocity through each node was calculated by determining the appropriate friction velocity—calculated in an iterative fashion. This was done by requiring the calculated mean velocity, Eq. (9) and the specified mean velocity (based on mass flux), Eq. (10) to be equal to each other. This methodology was adopted from [18].

$$u_{mean} = \frac{1}{H_{eq}} \left[\sum_{i=1}^{N} (u[i] L_{cv}[i]) + \sum_{i=1}^{N-1} (u_{tha}[i] L_{cv,tha}[i]) \right] \tag{9}$$

$$u_{mean} = \frac{G_{chan}}{\rho_{in}} \tag{10}$$

A total of 50 nodes were used to span a distance of 461.54 μm (equivalent height between the plates $D_h = 2 \times H_{eq}$ [19], where D_h is that of the microchannel). With a total of 50 nodes across the flow channel, the spacing between adjacent nodes in the near wall region, was smaller compared to the thickness of the sub-layer—allowing to obtain a high resolution temperature distribution in that region. Additionally, these nodes were distributed in a logarithmic fashion, with more nodes concentrated in the near wall region where the steepest gradients are to be expected. With the specified uniform heat flux, the wall temperature can be obtained from Eq. (11).

$$q''_{flux} = k_{eff}[1] \left(\frac{T_{w,b} - T_F[1]}{y[1]} \right) \tag{11}$$

The differential equation, used to obtain the axial temperature evolution of the first fluid node is given by Eq. (12)

$$\begin{aligned} \frac{dT_F[1]}{dx} = \Bigg\{ & k_{eff}[1] \left(\frac{T_{w,b} - T_F[1]}{y[1]} \right) \\ & - \left[\left(\frac{k_{eff}[1] + k_{eff}[2]}{2} \right) \left(\frac{T_F[1] - T_F[2]}{y[2] - y[1]} \right) \right] \Bigg\} \frac{1}{\rho[1] L_{cv}[1] u[1] c_p[1]} \end{aligned} \tag{12}$$

The differential equations for the interior fluid nodes for the bottom half of the channel, located between the first and channel center line node are as follows:

$$\frac{dT_F[i]}{dx} = \Bigg\{ \Bigg[\left(\frac{k_{eff}[i-1] + k_{eff}[i]}{2} \right) \left(\frac{T_F[i-1] - T_F[i]}{y[i] - y[i-1]} \right) \Bigg] - \Bigg[\left(\frac{k_{eff}[i] + k_{eff}[i+1]}{2} \right) \left(\frac{T_F[i] - T_F[i+1]}{y[i+1] - y[i]} \right) \Bigg] \Bigg\} \frac{1}{\rho[i] L_{cv}[i] u[i] c_p[i]} \tag{13}$$

The differential equation for the fluid node located at the channel center line is as follows:

$$\frac{dT_F[N]}{dx} = \Bigg\{ \Bigg[\left(\frac{k_{eff}[N-1] + k_{eff}[N]}{2} \right) \left(\frac{T_F[N-1] - T_F[N]}{y[N] - y[N-1]} \right) \Bigg] - \left(\frac{(k_{eff}[N] + K_{eff,th}[N-1]}{2} \right) \left(\frac{T_F[N] - T_{F,th}[N-1]}{y[N] - y[N-1]} \right) \Bigg] \Bigg\} \frac{1}{\rho[N] L_{cv}[N] u[N] c_p[N]} \tag{14}$$

The differential equations for the interior nodes in the channel top half, with the direction of heat transfer from bottom to top half, are as follows:

$$\frac{dT_{F,th}}{dx} = \Bigg\{ \Bigg[\left(\frac{k_{eff,th}[i+1] + k_{eff,th}[i]}{2} \right) \left(\frac{T_{F,th}[i+1] - T_{F,th}[i]}{y[i+1] - y[i]} \right) \Bigg] - \left(\frac{(k_{eff,th}[i] + K_{eff,th}[i-1]}{2} \right) \left(\frac{T_{F,th}[i] - T_{F,th}[i-1]}{y[i] - y[i-1]} \right) \Bigg] \Bigg\} \frac{1}{\rho_{tha}[i] L_{cv,tha}[i] u_{tha}[i] c_{p,tha}[i]} \tag{15}$$

Finally, the differential equation for the fluid node adjacent to the top wall of the channel is as follows:

$$\frac{dT_{F,th}[1]}{dx} = \left(\frac{k_{eff,th}[2] + k_{eff,th}[1]}{2} \right) \left(\frac{T_{F,th}[2] - T_{F,th}[1]}{y[2] - y[1]} \right) \times \frac{1}{u_{tha}[1] L_{cv,tha}[1] \rho_{tha}[1] c_{p,tha}[1] L_{cv,tha}[1]} \tag{16}$$

The adiabatic boundary condition at the channel top wall implies that the temperature of the fluid node adjacent to the top wall is equal to the channel top wall temperature, i.e.:

$$T_{F,th}[1] = T_{w,t} \tag{17}$$

These differential equations can then be integrated to obtain the local heat transfer coefficients. In this study, the calculation procedure was carried out using the Engineering Equation Solver (EES) [20] platform with the channel inlet temperature as the initial condition. During this integration process, the temperature dependent thermophysical properties for the current integration step are taken from those calculated at the previous step. This allows the iterative solver to converge when there is a drastic change in the thermophysical properties of sCO_2 in the proximity of the pseudo-critical point. After obtaining the thermal profile across the channel, the bulk fluid temperature can be calculated as shown in Eq. (20). Using the bulk fluid temperature, the local heat transfer coefficient and the Nusselt number is obtained according to Eq (21) and (22), respectively.

$$T_F[i] = T_{ch,in} + \int_{x=0}^{x=L_{ch}} \left(\frac{dT_F[i]}{dx}\right) dx \tag{18}$$

$$T_{F,th}[i] = T_{ch,in} + \int_{x=0}^{x=L_{ch}} \left(\frac{dT_{F,th}[i]}{dx}\right) dx \tag{19}$$

$$T_{bulk} = \frac{1}{u_{mean} H_{eq}} \left[\sum_{i=1}^{N} (u[i] T_F[i] L_{cv}[i]) + \sum_{i=1}^{N-1} (u_{tha}[i] T_{F,th}[i] L_{cv,tha}[i]) \right] \tag{20}$$

$$\alpha = \frac{q_{flux}}{T_{w,b} - T_{bulk}} \tag{21}$$

$$Nu_{bulk} = \frac{q_{flux} D_h}{k_{bulk}(T_{w,b} - T_{bulk})} \tag{22}$$

3.1. Evaluation of the Prediction Scheme

To gain confidence in the accuracy of the technique implemented in the previous section, the predicted heat transfer results are compared against a canonical case with a similar geometry and heat flux boundary conditions. Here, we consider an asymmetrically heated annulus formed between two concentric tubes, shown in Figure 4. In this configuration, the bottom wall of the flow channel, i.e., the inner tube wall, can be heated while the external tube wall can be kept adiabatic— mimicking the boundary conditions of interest in the current study. Additionally, in the limiting case of the radius of the internal tube approaching that of the external tube, the flow in the annulus can be treated as flow between parallel plates [15].

Heat transfer data for this particular configuration were published by Kays and Leung [21]. They developed a computational scheme to predict the turbulent heat transfer for a range of annular flow geometries. One of these cases reported data as $\frac{r_{outer}}{r_{inner}} \to 1$ with heating limited to a single wall. These computational investigations were validated by using experimental data for air (Prandtl number = 0.7).

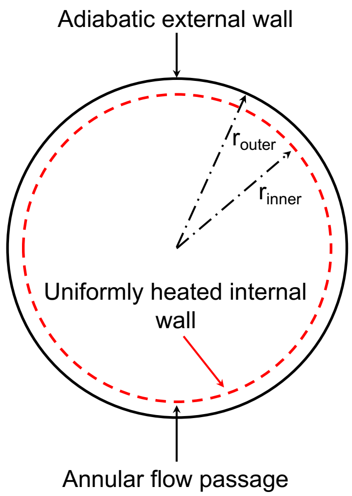

Figure 4: As $\frac{r_{outer}}{r_{inner}} \to 1$, the annulular flow geometry approaches that of parallel flat plates.

Using the model developed in our study, the local Nusselt numbers for sCO_2 were calculated for operating conditions away from the pseudo-critical point. For these conditions, no significant density gradients would be present in the flow channel, therefore the effects of both buoyancy and flow acceleration on eddy diffusivity are ignored. A turbulent Prandtl number of 0.9 was chosen, the same as that used by Kays and Leung [21] in their calculations. All other calculation details were similar to those described in the section 3. The inputs used for this evaluation of the model are summarized in Table 2. Using these inputs, the model is solved, providing a two-dimensional temperature distribution across the channel. A few of these temperature profiles are shown in Figure 5.

Table 2: Inputs to the predictive model to calculate the local Nusselt number for conditions away from the pseudo-critical point.

Nomenclature	Description	Numerical value
P_{inlet}	Absolute pressure of sCO_2	8900 kPa
Re_{inlet}	Reynolds number at inlet	3×10^4
T_{pc}	Pseudo-critical temperature	39.48^0C
T_{inlet}	Channel inlet temperature	45^0C
D_H	Hydraulic diameter for parallel plates	$2\times H_{eq}$
RR	Relative Roughness	0
$\triangle_{P,fric}$	Channel frictional pressure drop	1352 Pa
Pr_{inlet}	Inlet Prandtl number	1.62
Pr_{turb}	Turbulent Prandtl number	0.9

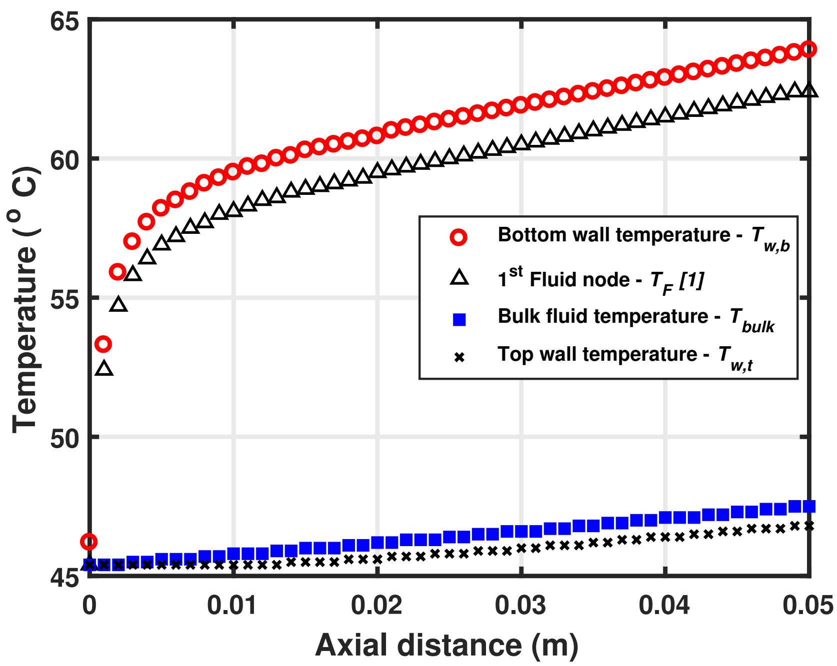

Figure 5: Temperature profiles obtained from the resistance network model developed for flow between parallel plates with asymmetric heating.

The Nusselt number data provided by Kays and Leung [21] are a function of Prandtl number. This data set was fitted with a third order polynomial and then used to obtain the Nusselt number variations along the channel length as a function of Prandtl evaluated at the wall temperature. Figure 6 shows the the results of the comparison of calculated local Nusselt numbers and those reported by Kays and Leung [21]. In the developing region, the maximum error between the model and the results of Kays and Leung is 57.1%. This difference decreases, on average, to is 3.3% in the fully developed region. The maximum deviation observed in the fully developed region is 3.81%. The average difference between these is 3.3% in the thermally fully developed region, giving credibility to the approach used to setup the predictive model.

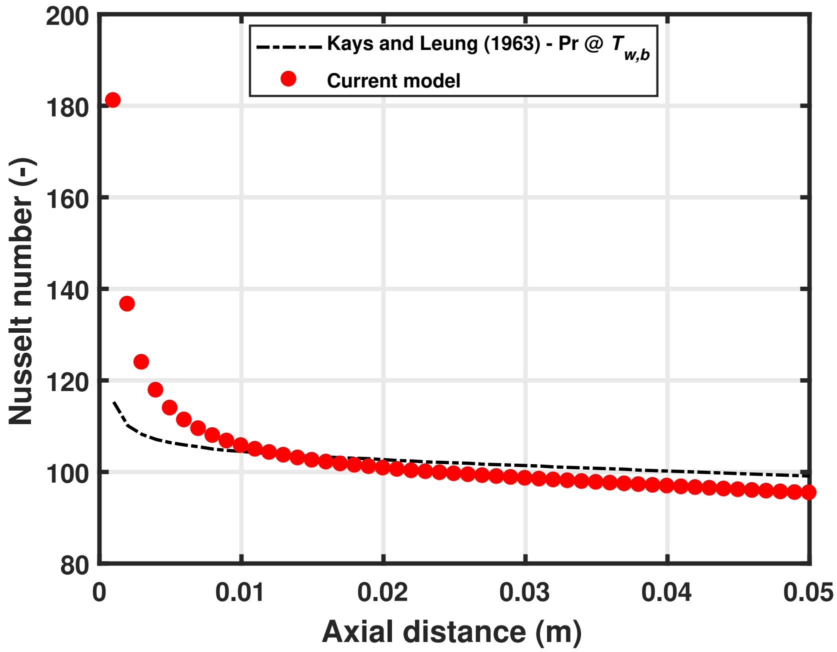

Figure 6: Comparison of local Nusselt numbers. In the thermally developed region (> 0.029 m), the average difference between the two trends is 3.3%.

3.2. Determining the Turbulent Prandtl Number

Turbulent Prandtl number can be a function of several flow parameters — velocity and temperature gradients, turbulent shear stress, turbulent heat flux, and stratification. Additionally, turbulent Prandtl number is not constant within the flow field, with the highest values observed close to the wall and can be as high as 2 for air ($Pr = 0.7$) [15]. Several authors have reported using variable values of turbulent Prandtl numbers to model the heat transfer of supercritical carbon dioxide in the proximity of the pseudo-critical point [22, 23, 24]. With many different factors influencing the turbulent Prandtl number, it is not possible to know the exact value before starting the calculation procedure. Therefore, the value of turbulent Prandtl number, used in the bottom half of the channel, was determined in an iterative fashion.

The values of the turbulent Prandtl number were changed in the model until the numerically predicted bulk temperature profile matched those predicted by a first law balance on the flow channel (within 0.1°C). This process is illustrated in the flow chart shown in Figure 7 and can be summarized in the following steps:

1. The inputs of heat flux, mass flux, absolute pressure, inlet bulk temperature, pseudo-critical temperature, and an estimate of the turbulent Prandtl number are entered in the model.

2. The model solves equations (1) through (22) to obtain the wall temperature and the bulk fluid temperature.

3. The bulk fluid temperature is compared to that obtained by the first law balance on the channel.

4. If the numerically predicted bulk temperature is within 0.1 °C of that obtained by the first law, the calculation procedure proceeds. If this is not the case, steps 1 through 4 are repeated with an updated value of the turbulent Prandtl number.

5. The calculation then proceeds to determine the heat transfer coefficients and the Nusselt number

Since the top half of the channel is not expected to be significantly affected by unstable stratification, a constant value was used there. Turbulent Prandtl number varies across the boundary layer and can be as high as 2 in the near wall region [15]. Therefore, a value of 1.9 was chosen to account for the limiting resistance of the near wall region in the top portion of the channel. Tang *et al.* [22] also reported, for supercritical carbon dioxide, increasing values of turbulent Prandtl number in the near wall region.

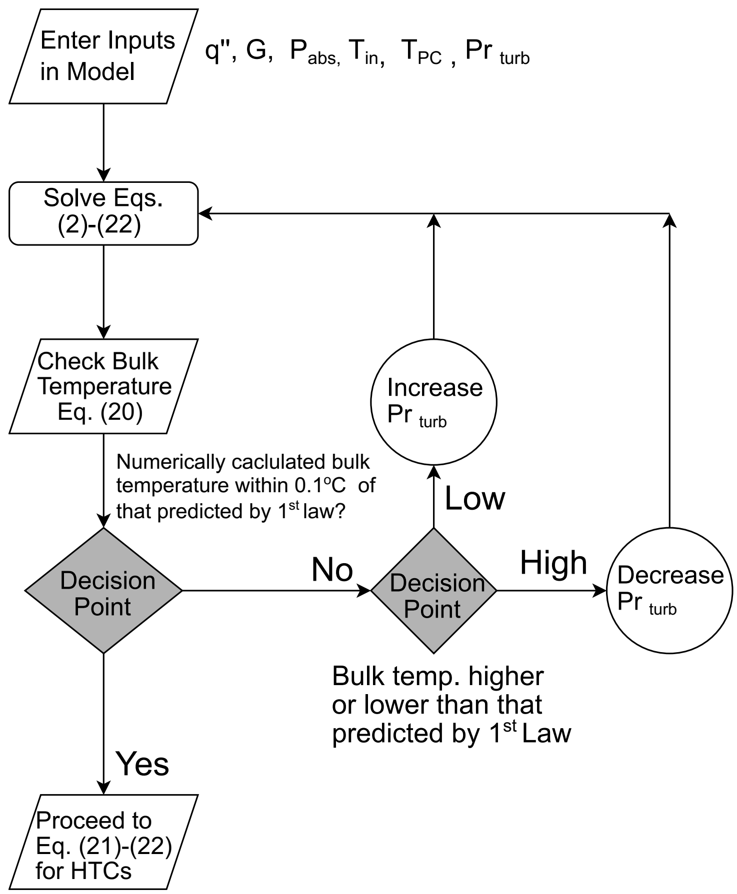

Figure 7: Flow chart illustrating the iterative scheme used to determine the correct turbulent Prandtl number used in the bottom half of the channel.

4. Comparison with Experimental Data

The predictions of the reduced order model are compared against data reported in [10]. In this comparison, the nominal channel mass flux ranges from 700 to 430 kg m^{-2} s^{-1} whereas the heat flux ranges from 5.7 to 11.1 W cm^{-2}. Unstable stratification and flow acceleration effects are expected to be present for channel mass fluxes below 500 kg m^{-2} s^{-1} and heat flux values higher than 7 W cm^{-2}, as predicted by the transition criteria of Petukhov [25] and Jackson [1].

Figure 8 shows the comparison for a nominal channel mass flux of 700 kg m^{-2} s^{-1}. The associated values of the turbulent Prandtl number and the $MAPE$ values are shown in Table 3. The comparison was started at an axial position of 2.4 mm. This was done to avoid comparison with the extremely high values of the heat transfer coefficients predicted by the model in the very first time steps of the solution. These very high heat transfer coefficients are not physical but rather an artifact of the numerical scheme used to solve the coupled set of ordinary differential equations.

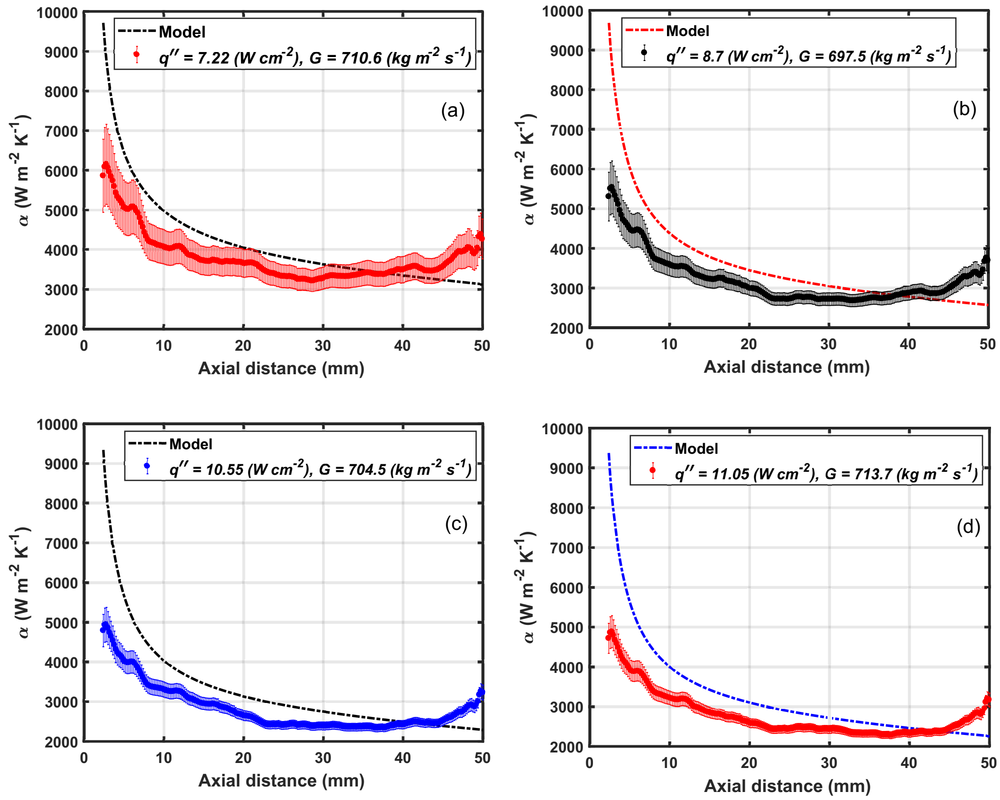

Figure 8: Comparison of the predictions of the reduced order model against the experimental data with a nominal channel mass flux of 700 kg m^{-2} s^{-1} and a nominal inlet temperature of 32.8°C. The comparison is started at an axial position of 2.4 mm instead of 0 mm.

Table 3: $MAPE$ values and turbulent Prandtl number details for nominal mass flux of 700 kg m^{-2} s^{-1}.

G_{chan} (kg m^{-2} s^{-1})	q'' (W cm^{-2})	Average $MAPE$ %	Pr_{turb} (-)
710.6	7.22	13.9	1.9 IF $\left(\frac{T_{Bulk}}{T_{PC}} < 0.999\right)$ ELSE 1.8
697.5	8.7	16.19	1.45 $\left(\frac{T_{Bulk}}{T_{PC}} > 0.999\right)$
704.4	10.55	17.7	1.15 $\left(\frac{T_{Bulk}}{T_{PC}} > 0.999\right)$
713.7	11.09	18.12	1.1 $\left(\frac{T_{Bulk}}{T_{PC}} > 0.999\right)$

The comparison of the model with the experimental data with a nominal channel mass flux of 460 kg m^{-2} s^{-1} is shown in Figure 9 and the details of the $MAPE$ and turbulent Prandtl number are summarized in Table 4. Again, as the heat flux is increased or the ratio, $\frac{T_{Bulk}}{T_{PC}}$ approaches unity, the values of the turbulent Prandtl number drop. Additionally, the $MAPE$, for all the cases in this data set, is below 20 %.

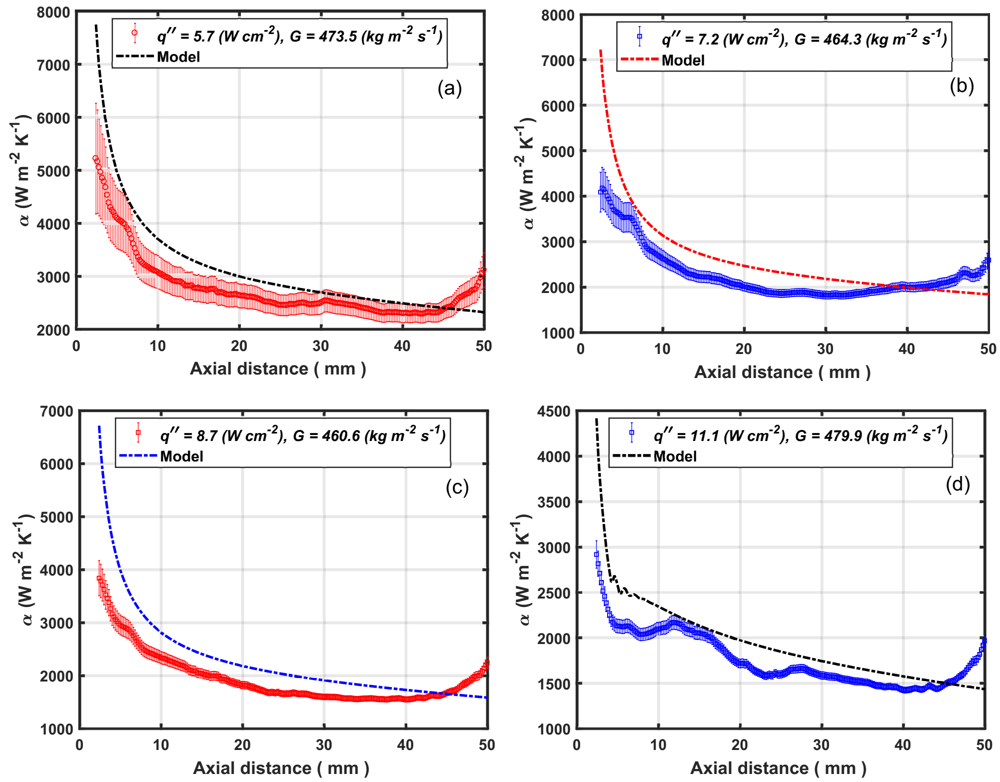

Figure 9: Comparison of the predictions of the reduced order model against the experimental data with a nominal channel mass flux of 460 kg m^{-2} s^{-1} and a nominal inlet temperature of 32.8°C. The comparison is started at an axial position of 2.4 mm instead of 0 mm.

Table 4: $MAPE$ values and turbulent Prandtl number details for nominal mass flux of 460 kg m^{-2} s^{-1}.

G_{chan} (kg m^{-2} s^{-1})	q'' (W cm^{-2})	Average $MAPE$ %	Pr_{turb} (-)
473.5	5.7	13.3	1.4 $\left(\frac{T_{Bulk}}{T_{PC}} > 0.999\right)$
464.3	7.2	17.6	1.05 $\left(\frac{T_{Bulk}}{T_{PC}} > 0.999\right)$
460.6	8.7	18.9	0.8 $\left(\frac{T_{Bulk}}{T_{PC}} > 0.999\right)$
479.9	11.1	11.59	1.8 IF $\left(\frac{T_{Bulk}}{T_{PC}} < 0.999\right)$ ELSE 0.57

The predictive capability of the model is compared against the experimental results with a nominal channel mass flux of 430 kg m^{-2} s^{-1}. The results are shown in Figure 10 and the $MAPE$ and turbulent Prandtl number values are summarized in Table 5. The $MAPE$ for all the cases in this data set was below 25%. Additionally, the turbulent Prandtl number values dropped as the heat flux was increased and the ratio, $\frac{T_{Bulk}}{T_{PC}}$ approached unity.

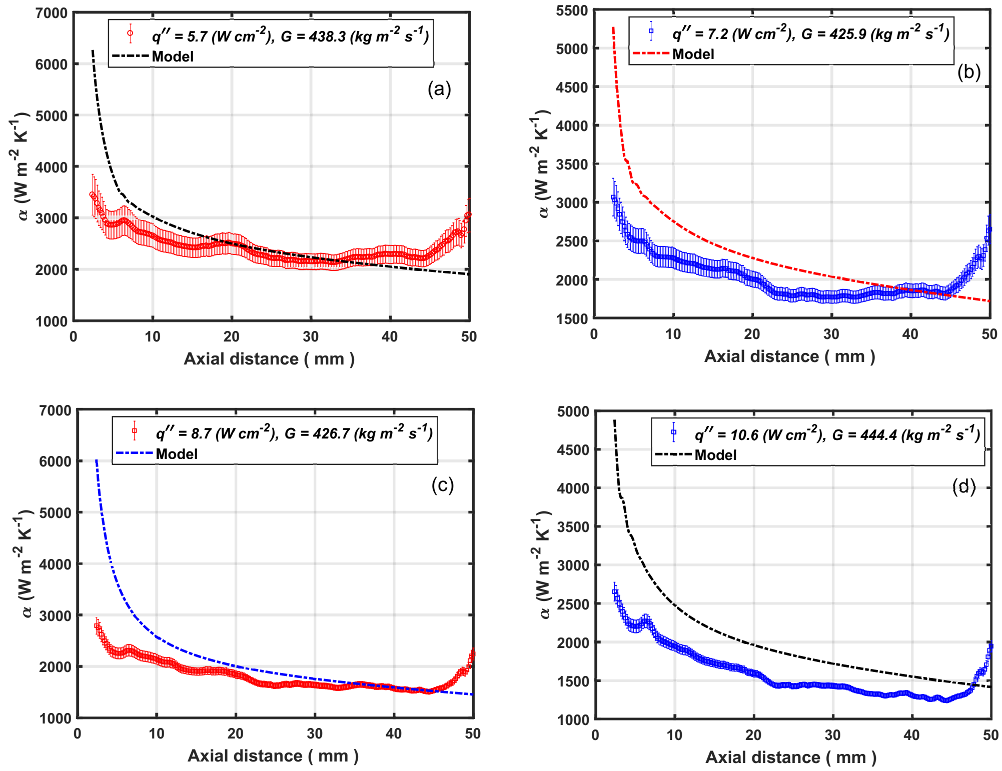

Figure 10: Comparison of the predictions of the reduced order model against the experimental data with a nominal channel mass flux of 430 kg m^{-2} s^{-1} and a nominal inlet temperature of 32.8°C. The comparison is started at an axial position of 2.4 mm instead of 0 mm.

Table 5: $MAPE$ values and turbulent Prandtl number details for nominal mass flux of 430 kg m^{-2} s^{-1}.

G_{chan} (kg m^{-2} s^{-1})	q'' (W cm^{-2})	Average $MAPE$ %	Pr_{turb} (-)
438.3	5.7	12.4	1.9 IF $\left(\frac{T_{Bulk}}{T_{PC}} < 0.999\right)$ ELSE 1.4
425.9	7.2	15.49	1.9 IF $\left(\frac{T_{Bulk}}{T_{PC}} < 0.999\right)$ ELSE 0.89
426.7	8.7	16.11	0.7 $\left(\frac{T_{Bulk}}{T_{PC}} > 0.999\right)$
444.4	10.6	24.7	1.9 IF $\left(\frac{T_{Bulk}}{T_{PC}} < 0.999\right)$ ELSE 0.52

The results of the comparison against the final experimental data set are shown in Figure 11. The $MAPE$ and the values of the turbulent Prandtl number for each individual case in this data set are summarized in Table 6. Apart from one case, the remaining cases in this data set had $MAPE$ values under 20%. Similar to the cases in the previous subsection, as the heat flux is increased or the ratio, $\frac{T_{Bulk}}{T_{PC}}$ approaches unity, the values of the turbulent Prandtl number drop.

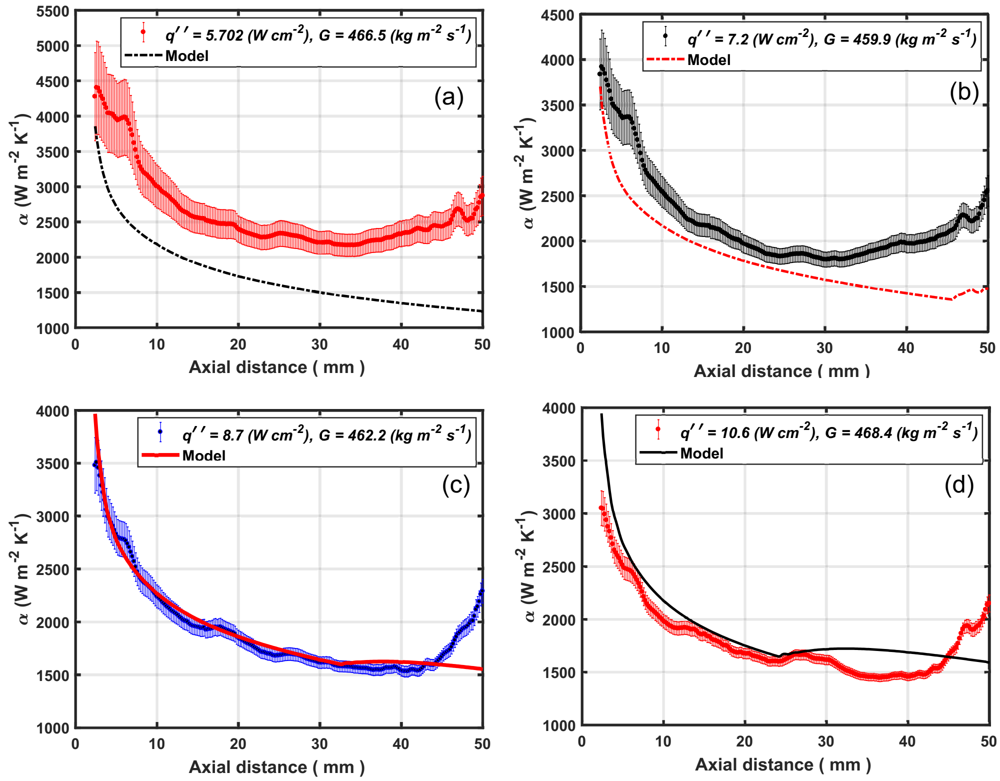

Figure 11: Comparison of the predictions of the reduced order model against the experimental data with a nominal mass flux of 460 kg m^{-2} s^{-1}.

Table 6: $MAPE$ values and turbulent Prandtl number details for test cases with a nominal mass flux of 460 kg m^{-2} s^{-1}.

G_{chan} (kg m^{-2} s^{-1})	q'' (W cm^{-2})	Average $MAPE$ %	Pr_{turb} (-)
466.5	5.7	34.18	$2.4 \left(\frac{T_{Bulk}}{T_{PC}} < 0.999\right)$
459.9	7.2	18.9	1.3 IF $\left(\frac{T_{Bulk}}{T_{PC}} < 0.999\right)$ ELSE 0.9
462.2	8.7	4.1	0.85 IF $\left(\frac{T_{Bulk}}{T_{PC}} < 0.999\right)$ ELSE 0.75
468.4	10.6	9.1	0.6 IF $\left(\frac{T_{Bulk}}{T_{PC}} < 0.999\right)$ ELSE 0.5

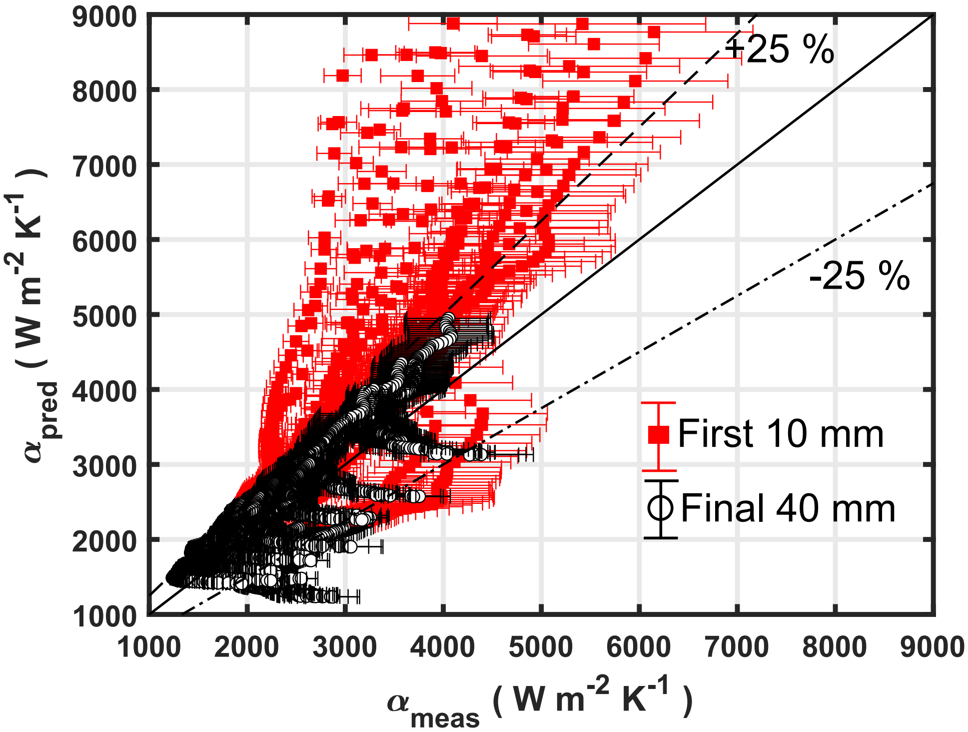

Figure 12: Comparison of the all the experimental data against the predictions of the model. The data has been split into two categories, the first 10 mm of the channel and the final 40 mm. In general, the model is able to predict the data with greater accuracy in the final 40 mm length of the channel

Generally, as the applied heat flux increased and the mass flux reduced, there was a reduction in the values of the turbulent Prandtl number. Also for each case, as the bulk fluid temperature approached the pseudo-critical temperature, the value of the turbulent Prandtl number dropped. Values specific to each case are tabulated along with the comparison results. A decreasing turbulent Prandtl number is an indication that the eddy diffusivity of heat is larger than the eddy diffusivity of momentum. Eddy diffusivity of heat is expected to increase as unstable stratification increases [16] and the molecular Prandtl number becomes larger which explains the observed reduction in the turbulent Prandtl number. Bazargan and Mohseni [24] report similar trends in the variations of the turbulent Prandtl number when buoyancy effects become significant. Additionally, the model developed in this section is able to predict the data with greater accuracy in the final 40 mm length of the channel. This can be seen in Figure 12.

4.1. Limitations of the Model

Although the current model provides an alternative to using CFD to model the supercritical heat transfer, there are some limitations inherent in the approach used. First, this methodology cannot be extended for constant temperature boundary conditions. For a constant temperature boundary condition, the turbulent Prandtl number cannot be calculated in an iterative fashion. Second, it was assumed that buoyancy and flow acceleration are not influencing the shape of the velocity profile. This is not accurate, particularly at high heat flux and low mass flux conditions. Mixed convective effects are known to distort the shape of the velocity profiles [25]. Finally, the current modeling approach can prove impractical when used to size a heat sink. Solving for the turbulent Prandtl number in an iterative fashion, as the operating conditions change, is computationally expensive and time consuming. On the other hand, a heat transfer correlation, as introduced below, is straightforward to implement and allows a thermal engineer to size a heat exchanger with ease.

5. Correlation Development

The correlation proposed here accounts for the following factors:

1. Developing length
2. Uniform single wall heating.
3. Variable thermophysical properties.
4. Flow acceleration.
5. Unstable stratification.

The correlation uses the Dittus and Boelter correlation [26] as a starting point, which captures the effect of Reynolds and Prandtl numbers on single-phase turbulent transport. However, due to varying thermophysical properties across the flow field, using bulk fluid temperature to evaluate the thermophysical properties is not appropriate. Reynolds number is to be evaluated as a function of the film temperature whereas the fluid thermal conductivity used in the Nusselt number should be evaluated as a function of wall temperature. The Prandtl number will be evaluated as a function of both the bulk fluid temperature and the wall temperature with the lowest of these values used in the correlation. Evaluating the thermal conductivity as a function of wall temperature and choosing the minimum value of the Prandtl number captures the effects of the near-wall diffusive region on the turbulent thermal transport. Minimum value of the Prandtl number has been used in the correlations proposed by Miropolskiy and Shitsman [27] and Ornastsky *et al.* [28].

A reduction in heat transfer coefficients has been reported for single-phase sub-critical turbulent flows in asymmetrically heated rectangular ducts [11]. A maximum reduction of 11% was reported in B.K. Rao's [11] study and therefore a constant of 0.89 is applied to the correlation developed in the current work. Additionally a factor, adopted from Nellis and Klein [18], is used to account for the effect of developing region on the predicted Nusselt number. This factor is defined in Eq. (23)

$$F_{dev} = \left[1 + \left(\frac{L_{ax}}{D_h}\right)^{-0.7}\right] \tag{23}$$

Flow acceleration is a consequence of an axial drop in the bulk fluid density under heating conditions. Since density depends upon temperature, if the axial temperature distribution is known, the magnitude of the thermally induced bulk flow acceleration can be determined. McEligot and Jackson [29] proposed a thermal loading parameter that accounts for the effect of flow acceleration on heat transfer. It is derived in the following fashion.

The bulk fluid temperature distribution inside a heated duct can be obtained by applying the first law balance on a control volume of length dx. This is shown in Eq. (24).

$$G_{chan}h_x + q''_{wall} = G_{chan}h_{x+dx} \tag{24}$$

$$G_{chan}h_x + q''_{wall} = G_{chan}h_x + G_{chan}\frac{dh_x}{dx}dx \tag{25}$$

$$q''_{wall} = G_{chan}\frac{dh_x}{dx} \tag{26}$$

Assuming that the fluid behaves as an ideal gas allows us to approximate $dh = c_p dT$, resulting in Eq. (27) which describes the change in fluid temperature for given value of channel mass flux and applied heat flux. Since, the axial density drop depends upon the bulk fluid temperature, this equation is also indicative of the expected flow acceleration for a given value of applied heat flux and channel mass flux. Dividing Eq. (27) by T_{bulk} on both sides, non-dimensionalizes the equation and results in a non-dimensional parameter, q^+.

$$\frac{q''_{wall}}{G_{chan}c_p} = dT \tag{27}$$

$$q^+ = \frac{q''_{wall}}{G_{chan}c_p T_{bulk}} \tag{28}$$

With the assumption that the fluid is behaving as an ideal gas, we can substitute Eq. (29) into Eq. (28), resulting in Eq. (30) which is called the thermal loading parameter [29].

$$\beta = \frac{1}{T_{bulk}} \tag{29}$$

$$q^+ = \frac{q''_{wall}\beta}{G_{chan}c_p} \tag{30}$$

Since in the current work, the heat flux is only limited to a single wall of the flow channel, the thermal loading parameter can be modified as shown in Eq. (31) [29]. The ratio of the heated to wetted perimeter accounts for the fact that the wall heat flux is not uniform across the channel periphery. The absolute magnitude of q^+ is indicative of the thermal acceleration expected to be present in the flow field.

$$q^+ = \frac{\beta q''_{wall}}{G_{chan}c_p}\left(\frac{Per_h}{Per_{wet}}\right) \tag{31}$$

Effects of unstable stratification on heat transfer will be accounted for by using the Richardson number as one of the non-dimensional numbers in the correlation. The Richardson number is defined in Eq.(32)

$$Ri = \frac{Gr_q}{Re_{film}^2} \tag{32}$$

$$Gr_q = \frac{g\bar{\beta}q''_{wall}D_h^4}{\nu^2 k_{bulk}} \tag{33}$$

$$\bar{\beta} = \frac{1}{\rho_{film}}\frac{\rho_{bulk} - \rho_{wall}}{T_{wall} - T_{bulk}} \tag{34}$$

Since flow acceleration and unstable stratification have the opposite influence on turbulent thermal transport, a single factor describing this relationship is defined in Eq.(35).

$$F_{Acc,Bo} = \frac{Ri}{q^+} \tag{35}$$

Based on the above discussion the correlation will take the form shown in Eq. (36) where x is an undetermined exponent, correlated from experimental data. A total of 15 experimental data sets with a unique combination of channel mass flux and heat flux, each consisting of 242 data points, were used to determine the value of the empirical exponent, x. The total error between the experimentally determined Nusselt number, defined in Eq. (37), and the one predicted by Eq. (36) was minimized using the method of quadratic approximations. The average value of x across all these data sets is 0.036 and therefore, the final form of the correlation is given in Eq. (38).

$$Nu_{wall} = F_{dev} \times 0.89 \times 0.023 Re_{film}^{0.8} Pr_{min}^{0.4} F_{Acc,Bo}^{x} \tag{36}$$

$$Nu_{exp} = \frac{\alpha_{exp} D_h}{k_{wall}} \tag{37}$$

$$Nu_{wall} = F_{dev} \times 0.89 \times 0.023 Re_{film}^{0.8} Pr_{min}^{0.4} F_{Acc,Bo}^{0.036} \tag{38}$$

Experimental data is available which was not used to determine the value of the exponent, x. This data can be used to assess the predictive capability of the proposed correlation. Four data sets, each with over 200 data points, were used for this comparison. The results of this comparison, and the $MAPE$ values for each data set, are shown in Figure 13. For all four data sets, the correlation predicted the experimental data with a $MAPE$ of under 22%.

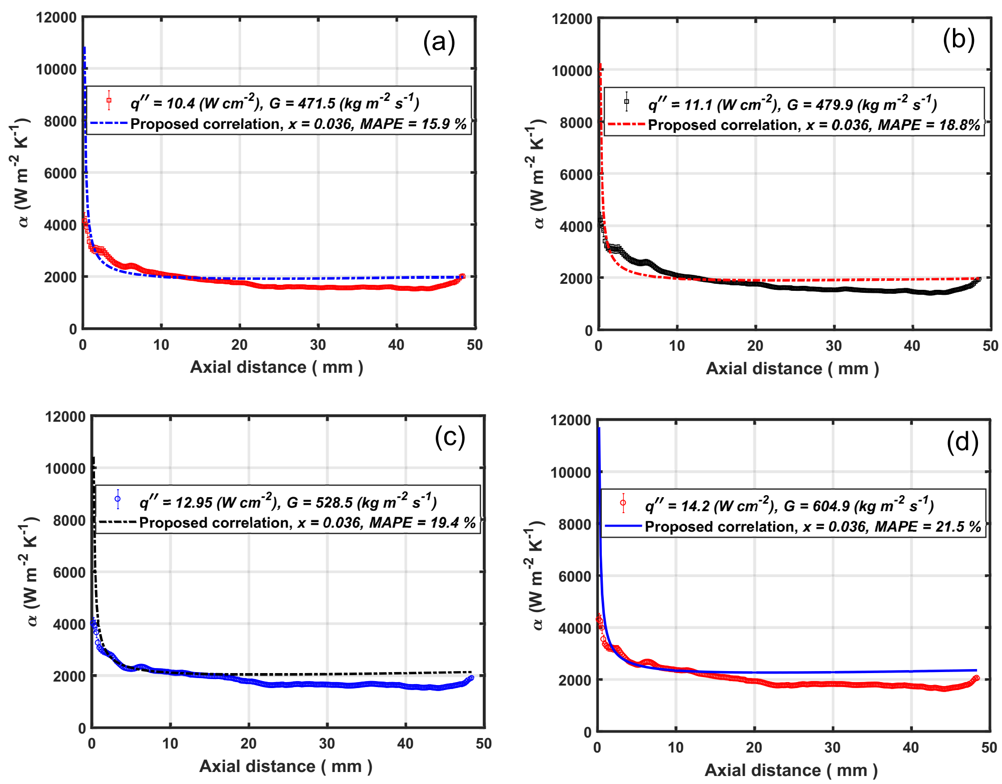

Figure 13: Comparison of the proposed correlation against local experimental data.

6. Conclusions

A reduced order model was developed to account for variable thermophysical property variations, flow acceleration, and unstable stratification. Variable thermophysical property variations across the boundary layer were accounted for by discretizing the resistance network model across and along the flow channel. Effects of flow channel acceleration were considered by using the Van-Driest expression for eddy diffusivity. Finally, the effects of unstable stratification manifested in the decreasing values of turbulent Prandtl number as the applied heat flux increased and channel mass flux decreased. The turbulent Prandtl number in the top half of the channel was kept constant at 1.9 while the one associated with the bottom half was allowed to vary.

The reduced order model was able to predict 14 out of 16 cases with a $MAPE$ of less than 20%. Generally, as the applied heat flux was increased and the channel mass flux reduced, the values of turbulent Prandtl number used in the model dropped. The lowest value used was 0.5. This is inline with the observations regarding the behavior of turbulent Prandtl number for unstable stratification conditions, as reported by Ueda *et al.* [16]. Additionally, within the flow channel, as the bulk temperature approached the pseudo-critical point and the molecular Prandtl number increased, the value of turbulent Prandtl number dropped.

This reduced order model can also be extended to predict the behavior of supercritical fluids, other than carbon dioxide, for similar operating conditions. However, a major limitation of the current modeling approach is that the iterative scheme used to calculate the turbulent Prandtl number will not work for constant temperature boundary condition. Additionally, if mixed convective effects were to become significant, the use of Spalding velocity profile might not be justified.

This study concludes with proposing a heat transfer design correlation that can be used to size heat sinks for use in electronics cooling applications.

This correlation accounts for the asymmetry in applied heating, unstable stratification, flow acceleration, and the effects of the developing region on supercritical heat transfer. The correlation predicted the experimental data with a $MAPE$ of under 22%.

7. Acknowledgements

The material presented in this paper is based upon work supported by the National Science Foundation under Grant No. 1604433. The authors also like to thank Greyson Termini for his help during the fabrication of the test section used in this study.

References

[1] J. D. Jackson, Fluid flow and convective heat transfer to fluids at supercritical pressure, Nuclear Engineering and Design 264 (2013) 24–40.

[2] J. D. Jackson, Heat transfer deterioration in tubes caused by bulk flow acceleration due to thermal and frictional influences (2012) 223–230.

[3] J. D. Jackson, Models of heat transfer to fluids at supercritical pressure with influences of buoyancy and acceleration, Applied Thermal Engineering 124 (2017) 1481–1491.

[4] I. L. Pioro, R. B. Duffey, Heat Transfer and Hydraulic Resistance at Supercritical Pressures in Power-Engineering Applications, ASME, 2007.

[5] I. L. Pioro, H. F. Khartabil, R. B. Duffey, Heat transfer to supercritical fluids flowing in channels - Empirical correlations (survey), Nuclear Engineering and Design 230 (2004) 69–91.

[6] M. B. Hyder, B. M. Fronk, Simulation of thermal hydraulic performance of multiple parallel micropin arrays for concentrating solar thermal applications with supercritical carbon dioxide, Solar Energy 164 (2018) 327–338.

[7] K. R. Zada, M. B. Hyder, M. Kevin Drost, B. M. Fronk, Numbering-Up of Microscale Devices for Megawatt-Scale Supercritical Carbon Dioxide Concentrating Solar Power Receivers, Journal of Solar Energy Engineering 138 (2016) 061007.

[8] B. M. Fronk, A. S. Rattner, High-Flux Thermal Management With Supercritical Fluids, Journal of Heat Transfer 138 (2016) 124501.

[9] M. Nabil, A. S. Rattner, Large eddy simulations of high-heat-flux supercritical CO2 convection in microchannels: Mixed convection and non-uniform heating, International Journal of Heat and Mass Transfer 145 (2019) 118710.

[10] S. A. Jajja, B. M. Fronk, Investigation of near-critical heat transfer in rectangular microchannels with single wall heating using infrared thermography, International Journal of Heat and Mass Transfer 177 (2021) 121470.

[11] B. K. Rao, Turbulent heat transfer performance of newtonian fluids in asymmetrically heated rectangular channels, Experimental Heat Transfer 2 (1989) 227–236.

[12] S. A. Jajja, K. R. Zada, B. M. Fronk, Experimental investigation of supercritical carbon dioxide in horizontal microchannels with non-uniform

heat flux boundary conditions, International Journal of Heat and Mass Transfer 130 (2019) 304–319.

[13] S. A. Jajja, B. M. Fronk, Experimental Data for Near Critical Turbulent Heat Transfer of Supercritical Carbon Dioxide in Rectangular Microchannels subject to Uniform Single Wall Heating, Figshare - (2020) https://doi.org/10.6084/m9.figshare.13262615.v1.

[14] L. V. Randle, B. M. Fronk, Investigation of Buoyancy Effects in Asymmetrically Heated Near-Critical Flows of Carbon Dioxide in Horizontal Microchannels Using Infrared Thermography, Proceedings of the ASME 2021 Heat Transfer Summer Conference June 16-18, Virtual, Online (2021) V001T11A0021 – V001T11A0027.

[15] W. M. Kays, M. Crawford, Convective Heat and Mass Transfer, McGraw-Hill, 2 edition, 1980.

[16] U. Hiromasa, S. Mitsumoto, S. Komoroi, Buoyancy effects on the turbulent transport processes in the lower atmosphere, Quarterly Journal of the Royal Meteorological Society 107 (1981) 561–578.

[17] D. B. Spalding, A single formula for the "law of the wall", Journal of Applied Mechanics, Transactions ASME 28 (1960) 455–458.

[18] G. Nellis, S. A. Klein, Heat Transfer, Cambridge University Press, 2012.

[19] A. Bejan, Convective Heat Transfer, John Wiley & Sons, 4 edition, 2013.

[20] S. Klein, F-Chart Software: EES, V10.104, 2016.

[21] W. Kays, E. Leung, Heat transfer in annular passages. Hydrodynamically developed laminar flow with arbitrarily prescribed wall temperatures or heat fluxes, International Journal of Heat and Mass Transfer 6 (1963) 537–557.

[22] H. S. Y. W. J. L. Z. L. Q. L. Tang, Guoli, H. Zhang, A variable turbulent Prandtl number model for simulating supercritical pressure CO2 heat transfer, International journal of heat and mass transfer 102 (2016) 1082–1092.

[23] Z. L. X. Y. M. C. J. Z. Y. R. Q. Q. Du, Xin, X. Zhu., Heat transfer of supercritical CO2 in vertical round tube: A considerate turbulent Prandtl number modification, Energy 192 (2020) 116612.

[24] M. Bazargan, M. Mohseni, Effect of turbulent Prandtl number on convective heat transfer to turbulent upflow of supercritical carbon dioxide., In Heat Transfer Summer Conference 43574 (2009) pp. 295–302.

[25] B. Petukhov, A. Polyakov, Heat Transfer in Turbulent Mixed Convection, Hemisphere Publishing Corporation, 1988.

[26] F. W. Dittus, L. Boelter, Heat Transfer in Automobile Radiators of the Tubular Type, Technical Report 13, University of California, 1930.

[27] Z. Miropol'ski, M. Shitsman, About calculation methods of heat transfer to water and steam at near-critical region (in Russian), Soviet Energy Technology 1 (1958) 8–11.

[28] A. Ornatsky, L. Glushchenko, E. Siomin, The research of temperature conditions of small diameter parallel tubes cooled by water un-

der supercritical pressures, in: Proceedings of the Fourth International Heat Transfer Conference, Paris-Versailles, France, Elsevier, Amsterdam, 1970.

[29] D. M. McEligot, J. D. Jackson, "Deterioration" criteria for convective heat transfer in gas flow through non-circular ducts, Nuclear Engineering and Design 232 (2004) 327–333.